JACS
JOURNAL OF THE AMERICAN CHEMICAL SOCIETY
pubs.acs.org/JACS
Article

Bright Fluorophores in the Second Near-Infrared Window: HgSe/CdSe Quantum Dots

Ananth Kamath, Richard D. Schaller, and Philippe Guyot-Sionnest*

Cite This: J. Am. Chem. Soc. 2023, 145, 10809−10816

Read Online
ACCESS | Metrics & More | Article Recommendations | Supporting Information

ABSTRACT: Fluorophores emitting in the NIR-IIb wavelength range (1.5−1.7 μm) show great potential for bioimaging due to their large tissue penetration. However, current fluorophores suffer from poor emission with quantum yields ∼2% in aqueous solvents. In this work, we report the synthesis of HgSe/CdSe core/shell quantum dots (QDs) emitting at 1.7 μm through the interband transition. Growth of a thick shell led to a drastic increase in the photoluminescence quantum yield, with a value of 63% in nonpolar solvents. The quantum yields of our QDs and other reported QDs are explained well by a model of Forster resonance energy transfer to ligands and solvent molecules. The model predicts a quantum yield >12% when these HgSe/CdSe QDs are solubilized in water. Our work demonstrates the importance of a thick type-I shell to obtain bright emission in the NIR-IIb region.

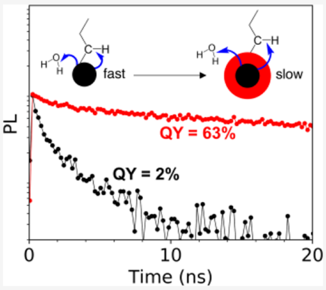

■ INTRODUCTION

Fluorophores in the second near-infrared (NIR-II) (1.3−2.3 μm) range have shown potential for noninvasive bioimaging due to reduced autofluorescence and significantly larger penetration into tissue compared to visible wavelengths.[1−6] The optimal wavelength for in-vivo imaging is the NIR-IIb range (1.5−1.7 μm) which allows the deepest penetration as a balance between reduced scattering and absorption by water.[1] In-vivo imaging in the NIR-II region has been demonstrated in imaging mouse brain vasculature,[7] lymph nodes,[1] and tumors.[2]

Several fluorophores have been developed for NIR-II bioimaging including organic molecules,[8,9] inorganic quantum dots,[1−3] and carbon nanotubes.[7,10] Despite significant progress, organic molecules show very low photoluminescence quantum yields (PLQYs) in the NIR due to their intramolecular vibrational relaxation to molecular vibrations by the energy gap law.[11,12] The brightest NIR fluorophores are based on inorganic quantum dots (QDs) which show QYs up to 43% at 1.5 μm emission.[13] However, the emission is quenched drastically when the QDs are solubilized in water, with QYs of ∼2% at 1.7 μm. Design of brighter QD fluorophores can lead to deeper penetration for in-vivo imaging, at lower excitation powers.[1]

The brightest reported QDs in the NIR-II range (1.3−2.3 μm) include QD structures based on PbS,[13−17] PbSe,[16] Ag_2S,[18] InAs,[2,19] HgTe,[20−23] and HgSe.[24,25] Nonradiative relaxation in QDs via surface trapping dominates the role in visible-gap QDs, while QDs in the infrared appear to be limited by a near-field Forster energy transfer to ligand molecules on the QD surface.[16,26] This is exacerbated on making the QDs water-soluble, as water is strongly absorbing and leads to a drastic decrease in the PLQY.[2]

The energy transfer can be suppressed by exchanging the organic ligands by less absorbing molecules, or by growth of a thick type-I shell.[25−27] Solid-state ligand exchange has been demonstrated in Ag_2S[18] and PbS[14,15] QD films, which show a PLQY of up to 85% at 1.4 μm. For in-vivo imaging, the only option is the growth of a thick shell, to suppress energy transfer to the surface ligand and solvent molecules. While thick CdS and CdSe shells have been grown on PbS[13] and PbSe[28] QDs, no substantial improvement in the PLQY is seen. Growth of the thick shell is also accompanied by a redshift of the exciton and lengthening of the PL lifetime,[28] which has been attributed to the quasi-type-II band alignment between the core and the shell.[13,28] Similar observations have been reported for InAs/CdSe QDs, where the PLQY does not improve with shell thickness due to the unfavorable band alignment.[2,29] This motivates the design of a core/shell material system with a type-I alignment to obtain bright fluorophores in the NIR-II region.

HgSe/CdS QDs show bright mid-infrared emission when n-doping through the intraband transition.[25] Undoped HgSe QDs show emission in the NIR-II range. In contrast to PbS,[13] PbSe,[28] and InAs,[2] HgSe has a type-I band alignment with CdS and CdSe,[25,30] which makes it a promising candidate as bright NIR-II fluorophores. CdSe is the ideal shell candidate for obtaining bright emission in HgSe due to the type-I band alignment and near-zero lattice mismatch. Previous studies have reported growth of a thin CdSe shell <∼1.5 nm

Received: February 28, 2023
Published: May 3, 2023

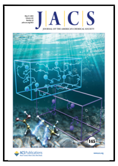

https://doi.org/10.1021/jacs.3c02190

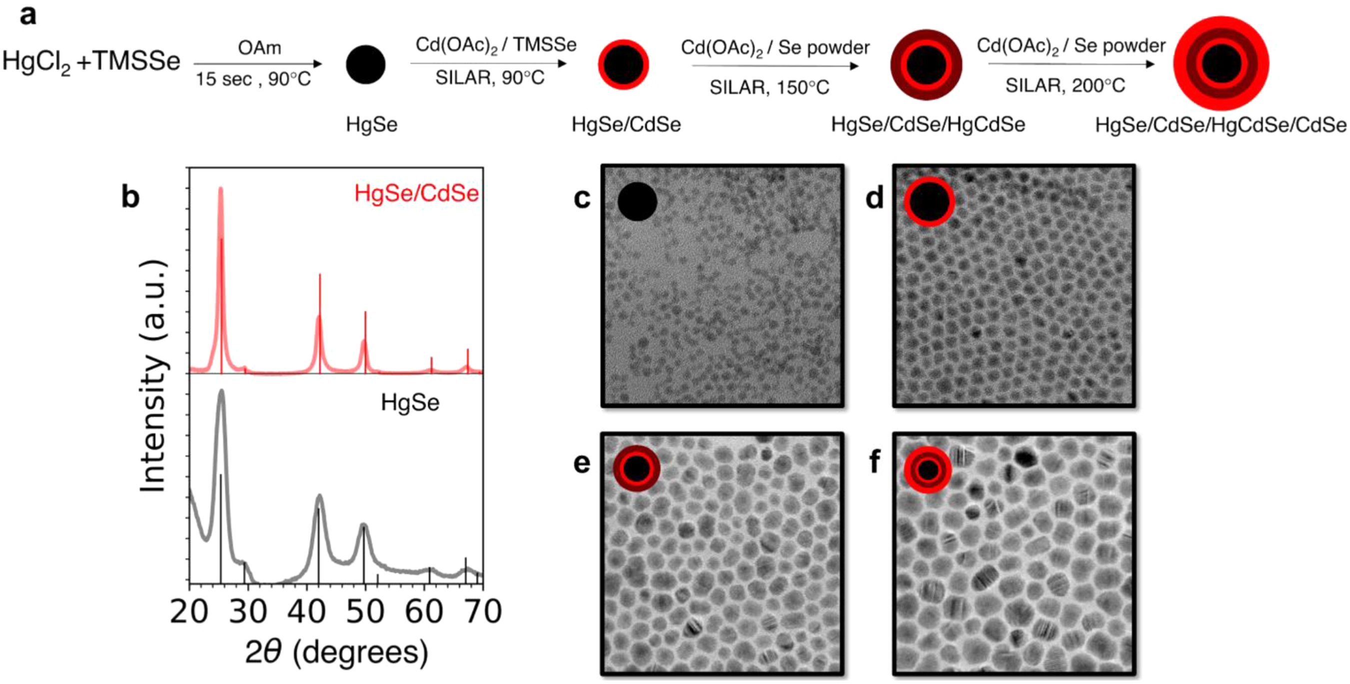

Figure 1. Synthesis of thick shell HgSe/CdSe QDs. (a) Schematic of synthesis of HgSe/CdSe QDs. HgSe cores were synthesized by hot injection of $HgCl_2$ and bis(trimethylsilyl)selenide ($(TMS)_2Se$) at 90 °C. A thin CdSe shell was then overcoated at 90 °C using cadmium acetate and $(TMS)_2Se$, by successive ion layer addition and reaction (SILAR). Subsequent shell growth was performed at 150 °C using cadmium acetate and selenium power. At this temperature, around 40−60% of the QDs dissolved and overcoated an alloyed HgCdSe shell around the remaining QDs. The final layers of CdSe were grown at 200 °C. (b) X-ray diffraction (XRD) spectra of 5.2 nm HgSe (black curve) and 15.1 nm HgSe/CdSe (red curve) QDs, along with calculated bulk XRD spectra for zincblende HgSe (black bars) and CdSe (red bars) with lattice constants 6.08 and 6.05 Å respectively. The spectra confirm the growth of CdSe along the zincblende crystal structure like the cores, and the near-zero lattice mismatch between the core and shell. (c−f) Transmission electron microscopy (TEM) images of HgSe and HgSe/CdSe QDs with a diameter of (c) 5.2 nm, (d) 7.0 nm, (e) 10.2 nm, and (f) 13.0 nm.

thickness,[24,30] but growth of a thick spherical shell was not achieved.

In this work, we show the growth of a thick, roughly spherical CdSe shell around HgSe QDs, up to a final QD diameter of 13 nm. These QDs exhibit a PLQY upto 63% at 1.7 μm wavelength, which is >3 times brighter than those reported previously. Our calculations show that the QYs are consistent with a Forster energy transfer to ligands and solvent molecules and demonstrate a strategy to obtain bright NIR-II fluorophores.

■ RESULTS AND DISCUSSION

Synthesis of HgSe/CdSe Core/Shell QDs. HgSe cores were synthesized by adapting a previous report.[31] The sizes of the QDs were characterized by transmission electron microscopy (TEM) and small angle X-ray scattering (SAXS). The cores had a diameter of 4.8−5.2 nm for emission at (1.7−2.0 μm) wavelengths. Most reports of CdSe growth require temperatures in excess of 200 °C to obtain large sizes.[28,32] Since HgSe QDs have poor thermal stability above 100 °C, it is necessary to first grow a thin protective CdSe shell at a low temperature before growth of a thick shell.[25] While previous studies report growth of thin shell HgSe/CdSe QDs using c-ALD,[24,30] the procedure is tedious, limited to small reaction scales, and is easily susceptible to independent nucleation.

In order to develop a robust and scalable growth of a thin CdSe shell at a low temperature, we designed a shell growth strategy using cadmium acetate and $(TMS)_2Se$ (Figure 1a). These precursors are highly reactive and form CdSe nanocrystals at temperatures as low as room temperature. By subsequent addition of Cd and Se layers by successive ionic layer adsorption and reaction (SILAR) at 90 °C, the shell thickness could be precisely controlled (SI Section 1C). The synthesis was robust and could be scaled up to 80 mg of HgSe, with little or no observed independent nucleation up to a thickness of three monolayers (SI Section 1C). After growth of three monolayers, the HgSe/CdSe QDs were thermally stable up to at least 150 °C, while the HgSe cores were not stable above 120 °C (SI Section 1D).

These thin shell HgSe/CdSe QDs were then used as seeds for growth of a thick CdSe shell. Synthesis of large core/shell nanocrystals requires the use of highly reactive precursors and a high reaction temperature in order to maintain a spherical shape and avoid independent nucleation.[25,32−34] We adapted the protocol by X Peng and coworkers, where they demonstrated growth of CdSe using cadmium carboxylates and selenium suspension in oleylamine, which decomposed at a low temperature of 140 °C.[35]

A major challenge during growth of the CdSe shell is ripening and dissolution of QDs with a thin CdSe shell, which leads to deposition of an alloyed HgCdSe shell on the remaining QDs.[25] While the optical properties of the surviving HgSe cores are not affected, the alloyed HgCdSe shell absorbs part of the excitation light during PL measurements. To minimize ripening and dissolution of the cores (SI Section 1G), we performed the shell growth through a two-step temperature increase. The reaction temperature was set to 150 °C for two CdSe monolayers, after which the temperature was increased to 200 °C or higher for subsequent shell growth (Figure 1a). During the heat-up to 150 °C, typically ~40 to

https://doi.org/10.1021/jacs.3c02190
J. Am. Chem. Soc. 2023, 145, 10809−10816

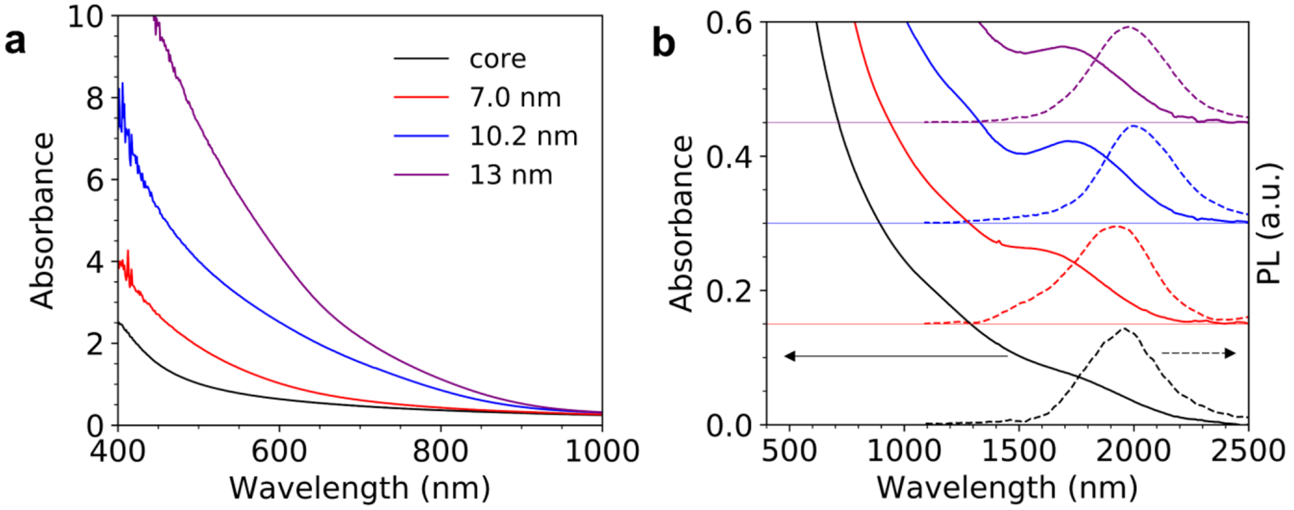

Figure 2. Absorption and PL. (a) Absorption spectra of 5.2 nm HgSe cores and HgSe/CdSe QDs with different sizes. All spectra are normalized at 1400 nm. The increasing band-edge absorption from the CdSe shell is evident from the absorption onset at 900 nm. (b) Absorption (solid) and photoluminescence (black) (PL) spectra of HgSe and HgSe/CdSe QDs. The absorptions have the same scale as in (a) but are vertically shifted for clarity. The absorption and PL spectra show negligible shift on shell growth, confirming the type-I band alignment of HgSe and CdSe.

60% of the QDs dissolved and deposited an alloyed shell around the remaining QDs (SI Section 3A).

Selection of the growth temperature is especially important. For obtaining thick spherical shells without independent nucleation, it is necessary to maximize the growth temperature.[25,33] We observe substantial independent nucleation during growth at 180 °C, which limits growth of QDs beyond 10 nm (Figure S1G-1). However, a higher growth temperature increases the tendency of alloying at the core/shell interface. We found the alloying temperature to depend on the core size. HgSe/CdSe QDs with cores emitting at 2.0 μm showed insignificant alloying during growth at 220 °C, but cores emitting at 1.7 μm show a large blueshift in absorption and photoluminescence when grown at the same temperature (Figure S1G-2). We thus set the growth temperature for 1.7 μm, emitting QDs as 200 °C. Using our synthetic design, we were able to obtain a final QD size of 13 nm at a growth temperature of 200 °C and a size of 16.5 nm at 220 °C (SI Section 1G).

Absorption Spectra and Optical Properties. An aliquot was taken after synthesis of HgSe cores at 15 s. The cores showed both interband absorption at 1.7 μm and an intraband absorption at 4.8 μm, which indicates that they are partially n-doped (SI Section 4A). By subtracting spectra of the cores at different dopings, we were able to calculate the average doping of the cores to be ~1.05 electrons/QD (SI Section 3B).

Aliquots were taken at different stages of the CdSe shell growth. Growth of the thick shell led to a steady increase in the CdSe absorption with a band-edge onset at 900 nm (Figure 2a). XRD measurements were performed on films of HgSe and HgSe/CdSe QDs (Figure 1b). The measured spectra show good agreement with simulated spectra for zincblende HgSe and CdSe. The Scherer sizes calculated for the (220) peak at 42° were 3.7 and 9.3 nm, respectively (SI Section 2E), which show a fair agreement with the sizes measured by SAXS.

The HgSe/CdSe QDs were intrinsic and showed negligible intraband transition, regardless of whether the final layer was Cd- or Se- (SI Section 1F). The thickest shell sample was an anomaly, which displayed an intraband absorption with roughly ~0.85 electrons/QD upon ending with a Cd step (SI Section 3B). The interband emission was much weaker after stopping at a Se- step (SI Section 1F), so all measurements were performed with Cd- as the final layer.

As seen from the absorption spectrum in Figure 2b, the absorption features of the HgSe interband transition were maintained on growth of the thick CdSe shell. During growth of the thick shell at 150 °C (Figure 2a, blue), there was a significant decrease in the HgSe absorption intensity (SI Section 3A) and a redshift of the absorption peak. This is consistent with dissolution of nearly half of the initial HgSe QDs and deposition of an alloyed shell around the remaining QDs. The redshift of the absorption suggests that thin shell HgSe/CdSe QDs with a smaller-sized core were preferentially dissolved. Subsequent growth of the CdSe shell did not result in a change in the absorption peak wavelength or intensity. The lack of peak shifting confirms the type-I band alignment between HgSe and CdSe. This is in contrast to PbS, PbSe, and InAs QDs, which show a continuous redshift in the exciton peak upon growth of a thick shell due to their quasi type-II band alignment.[2,13,28]

PL and Lifetime Measurements. Photoluminescence (PL) spectra of the HgSe/CdSe QDs were recorded using an excitation wavelength of 808 nm and an incident power of 15 mW, using a step-scan FTIR. All spectra were recorded in solution in tetrachloroethylene (TCE). The HgSe/CdSe QDs showed bright interband emission with no shift in the spectra on shell growth. There was a ~250 nm Stokes shift in the PL (~90 meV), which likely arises from the size distribution of the cores.

Absolute PL quantum efficiency measurements were performed using a Spectralon integrating sphere, with an 808 nm excitation and a PbSe detector. We want to distinguish the PL quantum efficiency (PLQE) from quantum yield (PLQY). When the sample has partial n-doping, there is an ensemble of QDs with 0, 1, and 2 electrons in the $1S_e$ state (denoted $1S_e(0)$, $1S_e(1)$, and $1S_e(2)$, respectively), each of which would have a specific PLQY. The absolute PLQE can be measured, but the PLQY would have to be calculated from the distribution of QDs with different $1S_e$ occupancies.[25] Only $1S_e(0)$ QDs would be expected to show interband emission

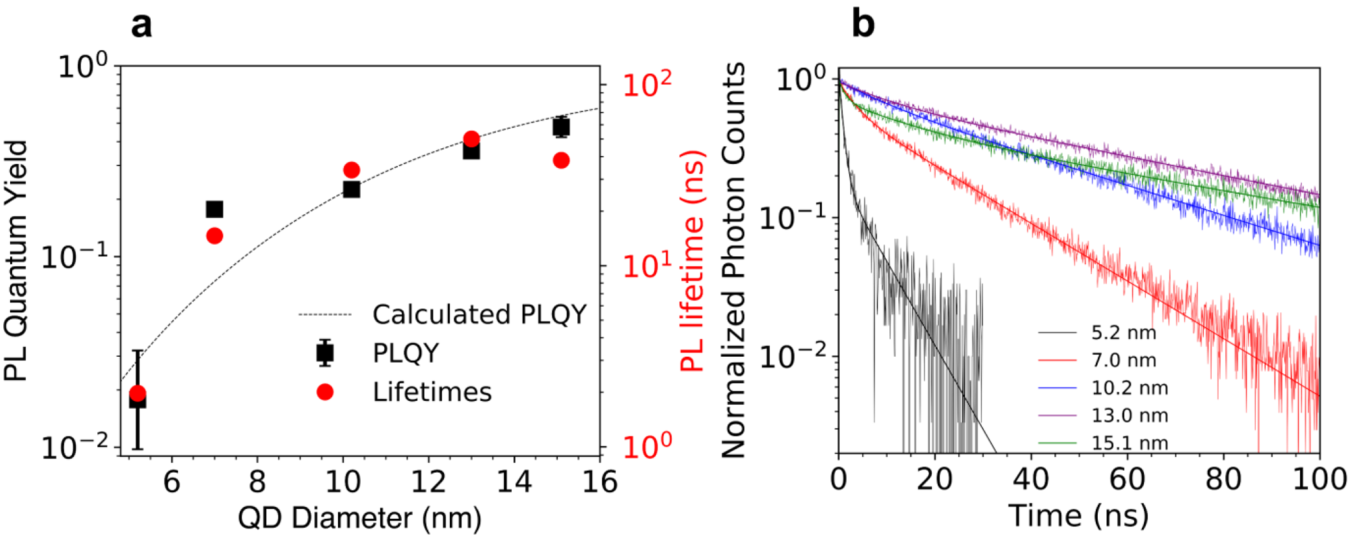

Figure 3. QY and lifetime measurements. (a) Measured PLQY (black squares) of HgSe/CdSe QDs with different shell thicknesses, calculated QY (dashed curve) modeled by Forster-energy transfer to oleylamine ligands on the QD surface, and measured average PL lifetimes (red circles). The increase in average lifetime with the QD size shows a quantitative agreement with the PLQY measurements. Error bars in PLQY correspond to lower and upper limits from the doping estimation. (b) PL lifetime traces (line scatter) of the same HgSe and HgSe/CdSe QDs in (a). The 15.1 nm sample was fit to a triexponential, while the remaining samples were fit to biexponentials (fits are overlayed).

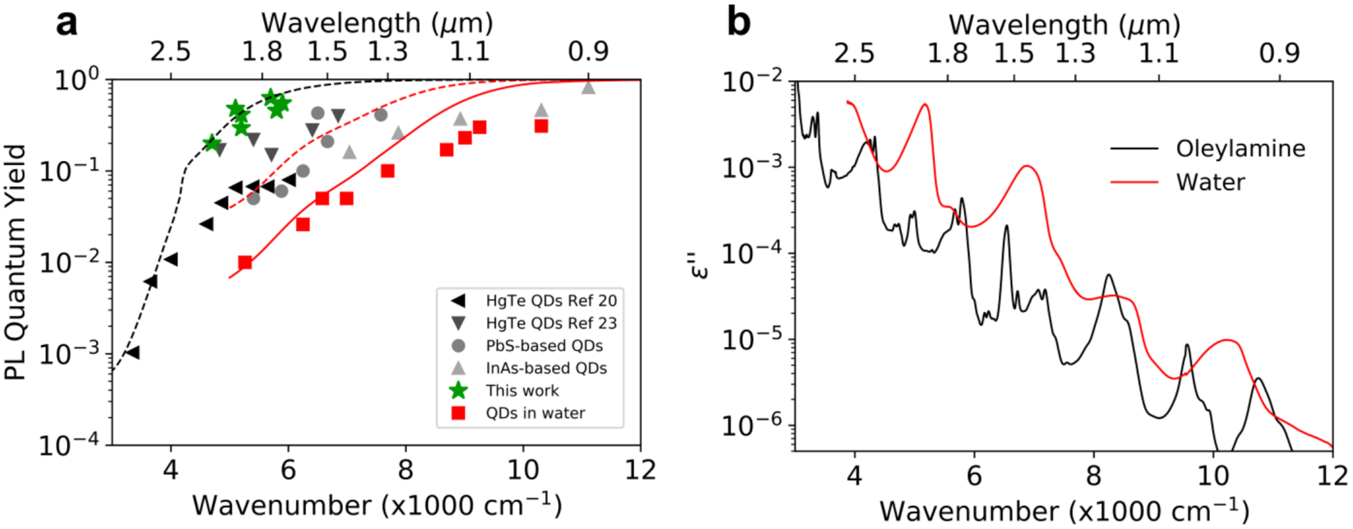

Figure 4. Predictions of the FRET model and comparison of PLQYs to other reports. (a) Compilation of PLQYs of the brightest reported QDs at different emission wavelengths. Black and gray points are QDs in organic solvents.[2,13,16,20,23] Red points are QDs solubilized in water for in-vivo imaging.[1−3,19,36] Green stars are our HgSe/CdSe QDs in nonpolar solvents. The curves are calculated PLQY by ligand-FRET to oleylamine in TCE (black) and including solvent-FRET in water (red). Solid curve is for 6 nm diameter QDs, and the dashed curve is for 13 nm diameter QDs. Ligand absorption and PLQY data are available in Supplementary Files. (b) Measured imaginary refractive index of oleylamine and water as a function of frequency. Absorption by water is nearly 5 times stronger than oleylamine.

due to Kasha's rule. To calculate the PLQY, we estimate the fraction of $1S_e(0)$ QDs in the ensemble by assuming a binomial distribution and divide the PLQE by this fraction (SI Section 3B).[25] Since only the cores and 15.1 nm HgSe/CdSe QDs were partially n-doped, the PLQE and PLQY were the same for QDs of the remaining sizes (SI Section 4A).

The HgSe cores showed a PLQY of 1.5% at 2.0 μm emission. Growth of the CdSe shell led to a monotonous increase in the PLQY, with a value of 48% for the thickest shell with a diameter of 15.1 nm (Figure 3a). A similar trend was observed for QDs with smaller cores emitting at 1.7 μm, which showed a PLQY upto 63% (SI Sections 3E and 4B). These QDs are >3 times brighter than the brightest fluorophores with PLQY ~20% at 1.7 μm emission.[23,24]

To confirm that the increase in the PLQY is indeed due to slowing of the nonradiative rate, we measured the PL lifetimes of HgSe and HgSe/CdSe QDs in solution (Figure 3b). With the exception of the 15.1 nm diameter sample, the lifetime traces of all samples fit well to a biexponential function. The fast component comprised ~25% of the intensity for the HgSe/CdSe QDs, while it was ~80% for the cores, which is likely due to a larger fraction of trap states in the cores. The 15.1 nm diameter sample was fit to a triexponential with ~30% intensity exhibiting very fast ~1.4 ns decay. We attribute this to defects arising from the independent nucleation of CdSe on the surface of the QDs (SI Section 4A).

We calculated the average PL lifetime to be a harmonic mean of the decay components (SI Section 4A and 4B). The trend of the effective PL lifetime showed quantitative agreement with the PLQY measurements (Figure 3a). From the measured lifetimes and PLQYs, we calculated the radiative lifetime for each QD sample. The radiative lifetime was similar for all QD samples, giving a value of 127 ± 30 ns. The constant radiative lifetime further confirms the type-I alignment of HgSe with CdSe.

Nonradiative Mechanism. QDs in the infrared show PLQYs that are lower than their visible counterparts. To determine the origin of the poor emission, we tabulated the PLQYs of the brightest reported QDs at different wavelengths (Figure 4a, data in Supplementary Files). We have plotted the PLQY of our HgSe/CdSe QDs emitting at different frequencies (Figure 4a, green stars). The QDs are ∼3 times brighter than previous QDs in the 1.7−2.0 μm range.

Despite the vast differences in the core and shell materials, all QDs in organic solvents (black and gray points) show a similar decreasing trend in the PLQY as the frequency is reduced. A similar trend is observed for QDs solubilized in water (Figure 4a, red squares), which have ∼5 times lower PLQYs than their counterparts in organic solvents. This general trend suggests that the PLQY is limited by a mechanism that depends on the emission frequency but is relatively insensitive to the QD material.

Guyot-Sionnest and coworkers[26] proposed a model for nonradiative relaxation involving Forster resonance energy transfer (FRET) of the QD emission to absorption of ligands on the QD surface. This model has been used to explain the lifetime and PLQY of QDs in the NIR and mid-IR regions.[16,20,25−27,37] In this model, the PLQY of QDs in nonpolar solvents is calculated as follows[37] (see SI Section 3D):

$$\frac{\gamma_{\mathrm{NR}}}{\gamma_{\mathrm{R}}} = \frac{3}{32\,\pi^3 n}\int_{R}^{R+\Delta R}\frac{\mathrm{d}r}{r^4}\int\frac{\epsilon''(\overline{\nu})f_{\mathrm{D}}(\overline{\nu})}{\overline{\nu}^3}\mathrm{d}\overline{\nu} \qquad (1)$$

where γ_{NR} is the nonradiative rate, γ_{R} is the radiative rate, n is the index of the solvent, R is the QD radius, ΔR is the ligand length, ϵ'' is the imaginary dielectric function of the ligand absorption, f_{D} is the normalized QD emission spectrum, and $\overline{\nu}$ is the frequency in wavenumbers.

The PLQY can be calculated as

$$\mathrm{PLQY} = \frac{\gamma_{\mathrm{R}}}{\gamma_{\mathrm{R}} + \gamma_{\mathrm{NR}}} = \frac{1}{1 + \frac{\gamma_{\mathrm{NR}}}{\gamma_{\mathrm{R}}}} \qquad (2)$$

Since the nonradiative rate is proportional to the radiative rate, the PLQY is independent of the radiative rate and hence insensitive to the QD material. This explains the relative insensitivity of the PLQY to the QD material. A notable exception is the series of HgTe QDs reported by Rogach and coworkers,[23] where the PLQY is higher and shows a weaker frequency dependence than other reports.

To calculate the ligand-FRET rate for QDs in nonpolar solvents, we measured the absorption spectrum of oleylamine (Figure 4b). Although the QD reports in Figure 4a have different nonpolar ligands, the FRET rate should be similar as the ligand absorption in the NIR-II is dominated by C-H overtones and combination bands (SI Section 3C). We used the reported surface coverage of oleylamine on the QD surface as 1.8 nm^{-2} (see SI Section 3D)[38] and set the emission spectra as Gaussians with a standard deviation 0.1 times the emission frequency. We calculated the FRET-limited PLQY as a function of the QD diameter (Figure 3a) and as a function of frequency by setting the QD diameter at 13 nm, which is the average size of the HgSe/CdSe QDs (Figure 4a dashed black curve).

The calculations show a good agreement with our measured PLQYs. The trend of calculated PLQY with frequency shows a reasonable agreement with the experimental data, with the scatter likely due to a variation in QD diameters, emission widths, different surface ligands, and contributions from other nonradiative processes.

Similar to ligands, FRET to solvent molecules can lead to a drastic quenching of the PLQY in NIR-absorbing solvents. To calculate the FRET rate to solvent molecules, we can use the solvent imaginary index ϵ'' in eq 1 and perform the integral from $R + \Delta R$ to infinity. To test the effect of solvent absorption on the nonradiative rate, we synthesized HgSe/CdSe QDs with an emission peak at 1.7 μm and measured the PLQY in TCE (tetrachloroethylene), CHCl$_3$, and octane. These solvents show an increasing absorption at the QD emission wavelength (Figure S3C(c),E(a)). The PLQY shows a monotonous decrease with the solvent absorption and shows good agreement with the simulation (SI Section 3E).

FRET to water is expected to play a major role for QDs optimized for in-vivo imaging. Water exhibits a strong broadband absorption in the NIR-II and leads to much poorer PLQYs compared to TCE. When we performed the FRET calculation for 6 nm diameter QDs, which is a typical size for water-solubilized QDs (Figure 4a, solid red curve), we find a good agreement with the reported PLQYs. Our calculation for 13 nm QDs in water predicts that the PLQY should be ∼12% at 1.7 μm emission (Figure 4a, dashed red curve), which is ∼6 times brighter than the brightest fluorophores reported.[1] Growth of 20 nm QDs should lead to a PLQY of ∼30% in water. While this is not currently possible with our synthetic protocol, further shell growth can be achieved by using a lower-temperature shell material like an HgCdSe alloy.

■ CONCLUSIONS

QDs emitting in the NIR-IIb range show great potential for in-vivo imaging, but the PLQY of the fluorophores are quite low (∼2%). To determine the origin of the fast nonradiative decay, we use a model of FRET to ligands and solvent molecules. Our calculation accounts for the ubiquitous decrease in the PLQY of QDs as the emission frequency is decreased and also explains the lower PLQY of QDs solubilized in water. Previous attempts to improve the PLQY have been unsuccessful due to the lack of a type-I core/shell system. In order to slow the nonradiative decay, we developed the synthesis of a thick CdSe shell on HgSe QDs. The type-I band alignment leads to a negligible spectral shift with increasing shell thickness. The thick shell HgSe/CdSe QDs show a PLQY upto 63% in the 1.7−2.0 μm range, which is ∼3 times brighter than the previous reported fluorophores. Our work demonstrates the importance of using thick shell QDs with a type-I band alignment for obtaining bright fluorophores.

■ METHODS

Thin Shell HgSe/CdSe QD Synthesis. The following protocol yielded ∼20 mg of HgSe cores. Briefly, HgCl$_2$ (0.1 mmol, 27 mg) was added to a three-neck flask with 5 mL of oleylamine. The flask was equipped with a stir bar, rubber sleeve stoppers with a thermocouple attached, and connected to an argon Schlenk line manifold. The flask was heated at 100 °C for ~30 to 60 min. The temperature was then set to 90 °C. $(TMS)_2Se$ solution (0.5 mL; 0.2 M) was injected swiftly into the flask. At 15 s, a calculated volume of 0.2 M $Cd(OAc)_2$ solution ("0Cd") was injected over a period of ~15 s. After 5 min, a calculated volume of 0.2 M $(TMS)_2Se$ solution ("1Se") was injected over a period of ~15 s. Subsequent cycles were performed as necessary, with a 2 min reaction time for Se cycles and 5 min reaction time for Cd cycles. Aliquots were taken if necessary using a glass syringe with a metal cannula. The reaction was typically stopped after 3 CdSe monolayers, leading to QDs with a diameter ~7 nm (denoted HgSe/3CdSe).

The stock solution was transferred into a glass vial and stored in a freezer. The stock solution was directly used for synthesis of a thick CdSe shell.

Thick Shell HgSe/CdSe QD Synthesis. The following protocol started with HgSe/3CdSe QDs containing 8 mg of HgSe. The fraction of QDs dissolved during the initial heat-up step was sensitive to the reaction scale.

HgSe/3CdSe stock solution from the freezer was fully thawed. A measured volume of the solution (containing 8 mg of HgSe) was added to a three-neck flask, equipped with a stir bar, rubber sleeves, a thermocouple, and connected to a Schlenk line. The solution was heated to 150 °C. A certain fraction (typically ~60%) of the QDs dissolved during the heat-up stage and deposited as an alloyed HgCdSe on the remaining QDs.

The Cd and Se precursor solutions were kept ready with 1 mL syringes. The Se- suspension was kept on the sonicator and mixed vigorously before adding the desired volume of the precursor. On reaching the set temperature, the Se precursor was added and left to react for 5 min. The Cd precursor was then added and left to react for 2 min. At this stage, the QD diameter was typically ~10.5 nm. One more Se and Cd cycle was performed. After the Cd addition, the temperature was set to 200 °C. Further Se and Cd cycles were performed, with a reaction time of 2 min for each cycle. Aliquots were taken if necessary using a glass syringe with a metal cannula. The QD diameters increased by roughly 0.7 nm per SeCd cycle. After ~13 nm, the QDs start to develop a tetrahedral-like morphology with a possibility of independent nucleation unless the reaction temperature is increased.

All samples were purified by two cycles of precipitation/dissolution using IPA and TCE.

Particle Size Characterizations. Transmission electron microscopy (TEM) images were recorded using an FEI Spirit 120 kV electron microscope and an FEI Tecnai F30 300 kV microscope.

SAXS measurements were performed using a SAXSLAB GANESHA instrument. The sample was prepared in a Kapton capillary tube and sealed.

XRD measurements were performed using a Rigaku Miniflex Benchtop spectrometer. Samples were dropcasted on a silicon holder.

Absorption and PL Measurements. UV–NIR absorption measurements in the 300–2500 nm range were performed using an Agilent Cary 5000 UMA spectrophotometer. Samples were prepared in a glass cuvette with 1 cm path length using TCE as the solvent.

FTIR absorption measurements in the 1600–10,000 nm range were performed using a ThermoNicolet iS50 spectrometer. Samples were prepared in a cell with CaF2 windows with 0.5 mm path length, using TCE as the solvent. FTIR measurements allowed a quantitative determination of the amount of HgSe cores in aliquots.

PL spectra were recorded using a step-scan FTIR spectrometer with an MCT detector and a gated integrator. The samples were excited with a 15 mW 808 nm diode laser, modulated at 90 kHz. A Si wafer was placed in front of the detector to block the excitation light. The transmittance of the solution at 808 nm was measured using a Si diode detector behind the sample cell.

Absolute PLQY measurements were performed on QD solutions in TCE in a CaF2 cuvette. The concentration of the solution was adjusted to keep the absorption of the 808 nm light between 20–80% to provide adequate signal while avoiding reabsorption of the PL (see Figure S2C-2).

The sample was placed in a Teflon integrating sphere (Thorlabs IS200-4), with the 808 nm laser excitation at one port, with a PbSe detector and Si diode detector at perpendicular ports (see Figure S2C-1). The 808 nm laser was modulated as a square wave at 1 kHz, with an average power of 15 mW. See SI Section 2C for details.

PL lifetime measurements were recorded using time-correlated single photon counting for samples in a 1 mm cuvette dispersed in TCE. Samples were excited with a Picoquant 50 ps pulsewidth laser diode operating at 976 nm and 1 MHz repetition rate. PL was collected with a lens, directed through a silicon long-pass filter, dispersed in a 0.3 m spectrograph set to pass the PL emission maximum, and detected with a Quantum Opus superconducting nanowire single photon detector. Single photon arrival times were collected as a histogram for 300 s with a timing bin resolution of 200 ps.

■ ASSOCIATED CONTENT

Supporting Information

The Supporting Information is available free of charge at https://pubs.acs.org/doi/10.1021/jacs.3c02190.

Detailed synthetic protocols; rationale for synthetic design; characterizations; spectroscopy measurement details; calculations; and raw data for QDs emitting at 1.7 and 2.0 μm (PDF)

Reported PLQY vs frequency (XLSX)

PLQE measurements (1.7 μm) (XLSX)

PLQE measurements (2.0 μm) (XLSX)

PLQY vs solvent (XLSX)

■ AUTHOR INFORMATION

Corresponding Author

Philippe Guyot-Sionnest − *Department of Chemistry and the James Franck Institute, The University of Chicago, Chicago, Illinois 60637, United States;* orcid.org/0000-0003-0178-6255; Email: pgs@uchicago.edu

Authors

Ananth Kamath − *Department of Chemistry and the James Franck Institute, The University of Chicago, Chicago, Illinois 60637, United States;* orcid.org/0000-0003-4740-5876

Richard D. Schaller − *Department of Chemistry, Northwestern University, Evanston, Illinois 60208, United States; Center for Nanoscale Materials, Argonne National Laboratory, Lemont, Illinois 60439, United States;* orcid.org/0000-0001-9696-8830

Complete contact information is available at: https://pubs.acs.org/10.1021/jacs.3c02190

Notes

The authors declare no competing financial interest.

■ ACKNOWLEDGMENTS

A.K. is grateful to Aritrajit Gupta for performing SAXS measurements and to Jennifer Hollingsworth for helpful discussions. A.K. thanks Chris Melnychuk for performing preliminary lifetime measurements. A.K. thanks Dmitri Talapin and Bozhi Tian for helpful inputs. A.K. thanks Lauren McNamara for sharing $CDCl_3$ for measurements. This work is supported by the U.S. DOE under award number DE-SC0023210. A.K. is supported by the Edith Barnard Memorial Fund from the Chemistry Department at the University of Chicago and by U.S. DOE DE-SC0023210. Work performed at the Center for Nanoscale Materials, a U.S. Department of Energy Office of Science User Facility, was supported by the U.S. DOE, Office of Basic Energy Sciences, under Contract No. DE-AC02-06CH11357. This work made use of the shared facilities at the University of Chicago Materials Research Science and Engineering Center, supported by National Science Foundation under award number DMR-2011854; the shared facilities at the University of Chicago Mass Spectrometry Facility, supported by National Science Foundation under award number CHE-1048528; and the University of Chicago electron microscopy facility (RRID:SCR_019198).

■ REFERENCES

(1) Wang, F.; Ren, F.; Ma, Z.; Qu, L.; Gourgues, R.; Xu, C.; Baghdasaryan, A.; Li, J.; Zadeh, I. E.; Los, J. W. N.; Fognini, A.; Qin-Dregely, J.; Dai, H. In Vivo Non-Invasive Confocal Fluorescence Imaging beyond 1,700 Nm Using Superconducting Nanowire Single-Photon Detectors. *Nat. Nanotechnol.* **2022**, *17*, 653−660.

(2) Franke, D.; Harris, D. K.; Chen, O.; Bruns, O. T.; Carr, J. A.; Wilson, M. W. B.; Bawendi, M. G. Continuous Injection Synthesis of Indium Arsenide Quantum Dots Emissive in the Short-Wavelength Infrared. *Nat. Commun.* **2016**, *7*, 12749.

(3) Zhang, M.; Yue, J.; Cui, R.; Ma, Z.; Wan, H.; Wang, F.; Zhu, S.; Zhou, Y.; Kuang, Y.; Zhong, Y.; Pang, D. W.; Dai, H. Bright Quantum Dots Emitting at ∼1,600 Nm in the NIR-IIb Window for Deep Tissue Fluorescence Imaging. *Proc. Natl. Acad. Sci. U. S. A.* **2018**, *115*, 6590−6595.

(4) Wang, F.; Wan, H.; Ma, Z.; Zhong, Y.; Sun, Q.; Tian, Y.; Qu, L.; Du, H.; Zhang, M.; Li, L.; Ma, H.; Luo, J.; Liang, Y.; Li, W. J.; Hong, G.; Liu, L.; Dai, H. Light-Sheet Microscopy in the near-Infrared II Window. *Nat. Methods* **2019**, *16*, 545−552.

(5) Jackson, C. T.; Jeong, S.; Dorlhiac, G. F.; Landry, M. P. Advances in Engineering Near-Infrared Luminescent Materials. *iScience* **2021**, *24*, No. 102156.

(6) Xia, F.; Gevers, M.; Fognini, A.; Mok, A. T.; Li, B.; Akbari, N.; Zadeh, I. E.; Qin-Dregely, J.; Xu, C. Short-Wave Infrared Confocal Fluorescence Imaging of Deep Mouse Brain with a Superconducting Nanowire Single-Photon Detector. *ACS Photonics* **2021**, *8*, 2800−2810.

(7) Hong, G.; Diao, S.; Chang, J.; Antaris, A. L.; Chen, C.; Zhang, B.; Zhao, S.; Atochin, D. N.; Huang, P. L.; Andreasson, K. I.; Kuo, C. J.; Dai, H. Through-Skull Fluorescence Imaging of the Brain in a New near-Infrared Window. *Nat. Photonics* **2014**, *8*, 723−730.

(8) Wan, H.; Yue, J.; Zhu, S.; Uno, T.; Zhang, X.; Yang, Q.; Yu, K.; Hong, G.; Wang, J.; Li, L.; Ma, Z.; Gao, H.; Zhong, Y.; Su, J.; Antaris, A. L.; Xia, Y.; Luo, J.; Liang, Y.; Dai, H. A Bright Organic NIR-II Nanofluorophore for Three-Dimensional Imaging into Biological Tissues. *Nat. Commun.* **2018**, *9*, 1171.

(9) Carr, J. A.; Franke, D.; Caram, J. R.; Perkinson, C. F.; Saif, M.; Askoxylakis, V.; Datta, M.; Fukumura, D.; Jain, R. K.; Bawendi, M. G.; Bruns, O. T. Shortwave Infrared Fluorescence Imaging with the Clinically Approved Near-Infrared Dye Indocyanine Green. *Proc. Natl. Acad. Sci. U. S. A.* **2018**, *115*, 4465−4470.

(10) Hong, G.; Lee, J. C.; Robinson, J. T.; Raaz, U.; Xie, L.; Huang, N. F.; Cooke, J. P.; Dai, H. Multifunctional in Vivo Vascular Imaging Using Near-Infrared II Fluorescence. *Nat. Med.* **2012**, *18*, 1841−1846.

(11) Freed, K. F.; Jortner, J. Multiphonon Processes in the Nonradiative Decay of Large Molecules. *J. Chem. Phys.* **1970**, *52*, 6272−6291.

(12) Friedman, H. C.; Cosco, E. D.; Atallah, T. L.; Jia, S.; Sletten, E. M.; Caram, J. R. Establishing Design Principles for Emissive Organic SWIR Chromophores from Energy Gap Laws. *Chem* **2021**, *7*, 3359−3376.

(13) Krishnamurthy, S.; Singh, A.; Hu, Z.; Blake, A. V.; Kim, Y.; Singh, A.; Dolgopolova, E. A.; Williams, D. J.; Piryatinski, A.; Malko, A. V.; Htoon, H.; Sykora, M.; Hollingsworth, J. A. PbS/CdS Quantum Dot Room-Temperature Single-Emitter Spectroscopy Reaches the Telecom O and S Bands via an Engineered Stability. *ACS Nano* **2021**, *15*, 575−587.

(14) Pradhan, S.; Dalmases, M.; Taghipour, N.; Kundu, B.; Konstantatos, G. Colloidal Quantum Dot Light Emitting Diodes at Telecom Wavelength with 18% Quantum Efficiency and Over 1 MHz Bandwidth. *Adv. Sci.* **2022**, *9*, No. 2200637.

(15) Pradhan, S.; Di Stasio, F.; Bi, Y.; Gupta, S.; Christodoulou, S.; Stavrinadis, A.; Konstantatos, G. High-Efficiency Colloidal Quantum Dot Infrared Light-Emitting Diodes via Engineering at the Supra-Nanocrystalline Level. *Nat. Nanotechnol.* **2019**, *14*, 72−79.

(16) Semonin, O. E.; Johnson, J. C.; Luther, J. M.; Midgett, A. G.; Nozik, A. J.; Beard, M. C. Absolute Photoluminescence Quantum Yields of IR-26 Dye, PbS, and PbSe Quantum Dots. *J. Phys. Chem. Lett.* **2010**, *1*, 2445−2450.

(17) Tsukasaki, Y.; Morimatsu, M.; Nishimura, G.; Sakata, T.; Yasuda, H.; Komatsuzaki, A.; Watanabe, T. M.; Jin, T. Synthesis and Optical Properties of Emission-Tunable PbS/CdS Core-Shell Quantum Dots for in Vivo Fluorescence Imaging in the Second near-Infrared Window. *RSC Adv.* **2014**, *4*, 41164−41171.

(18) Vasilopoulou, M.; Kim, H. P.; Kim, B. S.; Papadakis, M.; Ximim Gavim, A. E.; Macedo, A. G.; Jose da Silva, W.; Schneider, F. K.; Mat Teridi, M. A.; Coutsolelos, A. G.; bin Mohd Yusoff, A. R. Efficient Colloidal Quantum Dot Light-Emitting Diodes Operating in the Second near-Infrared Biological Window. *Nat. Photonics* **2020**, *14*, 50−56.

(19) Bruns, O. T.; Bischof, T. S.; Harris, D. K.; Franke, D.; Shi, Y.; Riedemann, L.; Bartelt, A.; Jaworski, F. B.; Carr, J. A.; Rowlands, C. J.; Wilson, M. W. B.; Chen, O.; Wei, H.; Hwang, G. W.; Montana, D. M.; Coropceanu, I.; Achorn, O. B.; Kloepper, J.; Heeren, J.; So, P. T. C.; Fukumura, D.; Jensen, K. F.; Jain, R. K.; Bawendi, M. G. Next-Generation in Vivo Optical Imaging with Short-Wave Infrared Quantum Dots. *Nat. Biomed. Eng.* **2017**, *1*, No. 0056.

(20) Keuleyan, S.; Kohler, J.; Guyot-Sionnest, P. Photoluminescence of Mid-Infrared HgTe Colloidal Quantum Dots. *J. Phys. Chem. C* **2014**, *118*, 2749−2753.

(21) Tenney, S. M.; Vilchez, V.; Sonnleitner, M. L.; Huang, C.; Friedman, H. C.; Shin, A. J.; Atallah, T. L.; Deshmukh, A. P.; Ithurria, S.; Caram, J. R. Mercury Chalcogenide Nanoplatelet−Quantum Dot Heterostructures as a New Class of Continuously Tunable Bright Shortwave Infrared Emitters. *J. Phys. Chem. Lett.* **2020**, *11*, 3473−3480.

(22) Kovalenko, M. V.; Kaufmann, E.; Pachinger, D.; Roither, J.; Huber, M.; Stangl, J.; Hesser, G.; Schäffler, F.; Heiss, W. Colloidal HgTe Nanocrystals with Widely Tunable Narrow Band Gap Energies: From Telecommunications to Molecular Vibrations. *J. Am. Chem. Soc.* **2006**, *128*, 3516−3517.

(23) Abdelazim, N. M.; Zhu, Q.; Xiong, Y.; Zhu, Y.; Chen, M.; Zhao, N.; Kershaw, S. V.; Rogach, A. L. Room Temperature Synthesis of HgTe Quantum Dots in an Aprotic Solvent Realizing High Photoluminescence Quantum Yields in the Infrared. *Chem. Mater.* **2017**, *29*, 7859−7867.

(24) Sagar, L. K.; Walravens, W.; Maes, J.; Geiregat, P.; Hens, Z. HgSe/CdE (E = S, Se) Core/Shell Nanocrystals by Colloidal Atomic Layer Deposition. *J. Phys. Chem. C* **2017**, *121*, 13816−13822.

(25) Kamath, A.; Melnychuk, C.; Guyot-Sionnest, P. Toward Bright Mid-Infrared Emitters Thick-Shell n-Type HgSe-CdS Nanocrystals. *J. Am. Chem. Soc.* **2021**, *143*, 19567−19575.

(26) Guyot-Sionnest, P.; Wehrenberg, B.; Yu, D. Intraband Relaxation in CdSe Nanocrystals and the Strong Influence of the Surface Ligands. *J. Chem. Phys.* **2005**, *123*, No. 074709.

(27) Guyot-Sionnest, P.; Pandey, A. Slow Electron Cooling in Colloidal Quantum Dots. *Science* **2008**, *322*, 929−932.

(28) Lee, D. C.; Robel, I.; Pietryga, J. M.; Klimov, V. I. Infrared-Active Heterostructured Nanocrystals with Ultralong Carrier Lifetimes. *J. Am. Chem. Soc.* **2010**, *132*, 9960−9962.

(29) Sagar, L. K.; Bappi, G.; Johnston, A.; Chen, B.; Todorović, P.; Levina, L.; Saidaminov, M. I.; García De Arquer, F. P.; Nam, D. H.; Choi, M. J.; Hoogland, S.; Voznyy, O.; Sargent, E. H. Suppression of

Auger Recombination by Gradient Alloying in InAs/CdSe/CdS QDs. *Chem. Mater.* **2020**, *32*, 7703−7709.

(30) Shen, G.; Guyot-sionnest, P. HgTe/CdTe and HgSe/CdX (X = S, Se, and Te) Core/Shell Mid- Infrared Quantum Dots. *Chem. Mater.* **2019**, *31*, 286−293.

(31) Melnychuk, C.; Guyot-Sionnest, P. Auger Suppression in N-Type HgSe Colloidal Quantum Dots. *ACS Nano* **2019**, *13*, 10512−10519.

(32) Hanson, C. J.; Hartmann, N. F.; Singh, A.; Ma, X.; Debenedetti, W. J. I.; Casson, J. L.; Grey, J. K.; Chabal, Y. J.; Malko, A. V.; Sykora, M.; Piryatinski, A.; Htoon, H.; Hollingsworth, J. A. Giant PbSe/CdSe/CdSe Quantum Dots: Crystal-Structure-Defined Ultrastable Near-Infrared Photoluminescence from Single Nanocrystals. *J. Am. Chem. Soc.* **2017**, *139*, 11081−11088.

(33) Chen, Y.; Vela, J.; Htoon, H.; Casson, J. L.; Werder, D. J.; Bussian, D. A.; Klimov, V. I.; Hollingsworth, J. A. "Giant" Multishell CdSe Nanocrystal Quantum Dots with Suppressed Blinking. *J. Am. Chem. Soc.* **2008**, *130*, 5026−5027.

(34) Zhao, H.; Sirigu, G.; Parisini, A.; Camellini, A.; Nicotra, G.; Rosei, F.; Morandi, V.; Zavelani-Rossi, M.; Vomiero, A. Dual Emission in Asymmetric "Giant" PbS/CdS/CdS Core/Shell/Shell Quantum Dots. *Nanoscale* **2016**, *8*, 4217−4226.

(35) Lai, R.; Pu, C.; Peng, X. On-Surface Reactions in the Growth of High-Quality CdSe Nanocrystals in Nonpolar Solutions. *J. Am. Chem. Soc.* **2018**, *140*, 9174−9183.

(36) Zhong, Y.; Ma, Z.; Wang, F.; Wang, X.; Yang, Y.; Liu, Y.; Zhao, X.; Li, J.; Du, H.; Zhang, M.; Cui, Q.; Zhu, S.; Sun, Q.; Wan, H.; Tian, Y.; Liu, Q.; Wang, W.; Garcia, K. C.; Dai, H. In Vivo Molecular Imaging for Immunotherapy Using Ultra-Bright near-Infrared-IIb Rare-Earth Nanoparticles. *Nat. Biotechnol.* **2019**, *37*, 1322−1331.

(37) Liu, H.; Guyot-Sionnest, P. Photoluminescence Lifetime of Lead Selenide Colloidal Quantum Dots. *J. Phys. Chem. C* **2010**, *114*, 14860−14863.

(38) Anderson, N. C.; Owen, J. S. Soluble, Chloride-Terminated CdSe Nanocrystals: Ligand Exchange Monitored by 1H and 31P NMR Spectroscopy. *Chem. Mater.* **2013**, *25*, 69−76.